Supplementary Information for

Large Spin Polarization from Symmetry-Breaking Antiferromagnets in Antiferromagnetic Tunnel Junctions

Chung-Tao Chou, Supriya Ghosh, Brooke C. McGoldrick, Thanh Nguyen, Gautam Gurung, Evgeny Y. Tsymbal, Mingda Li, K. Andre Mkhoyan, and Luqiao Liu*

*E-Mail: luqiao@mit.edu

Contents:

Section 1. Density-functional theory calculations for Mn_3Sn spin polarization

It is known that non-collinear antiferromagnetic (AFM) metals exhibit an uncompensated transport spin polarization along certain crystallographic directions (even in those cases when they do not have a relativistically-induced net magnetic moment) and therefore can perform as ferromagnets in magnetic tunnel junctions (MTJs) (e.g., Ref. 1, 2). Fig. S1(a) shows the atomic and magnetic structure of bulk Mn_3Sn. It has a hexagonal structure of space group $P6_3$/mmc with magnetic moments of Mn atoms lying in the (001) plane and forming a triangular lattice. They are rotated by 120° with respect to each other creating a non-collinear AFM configuration [3]. Such magnetic alignment belongs to a magnetic space group $Cmc'm'$ that has PT and $U\tau$ (U is spin rotation and τ is half a unit cell translation) symmetries broken. The broken PT and $U\tau$ symmetries ensure a spin-split electronic band structure of Mn_3Sn. It has three Fermi surface sheets, each revealing finite momentum-dependent spin expectation values [4] and thus momentum-dependent spin polarization [5, 6]. The net spin polarization depends on the transport direction, and, in general, it is not vanishing unless there is symmetry enforcing it to be zero.

As an example, we consider the [001] transport direction in Mn_3Sn. Figure S1(b) shows distribution of the spin expectation values for one of the three bands crossing the Fermi energy projected to the (001) 2D Brillouin zone (2DBZ). While overall the spin textures $\langle s_x \rangle$ and $\langle s_y \rangle$ are complex [$\langle s_y \rangle = 0$ for the (001) plane by symmetry], reflecting the intricate spin-polarized band structure of Mn_3Sn, there are certain symmetry properties in these textures that are notable. Specifically, the magnetic space group of Mn_3Sn has inversion symmetry P, mirror reflection combined with time reversal TM_z, mirror reflection M_x, and time reversal combined with mirror reflection and translation $\{TM_y \mid \tau = c/2\}$, the latter two being indicated in Figure S1(a). These symmetry constraints enforce $\langle s_x \rangle$ to be symmetric with respect to k_x and k_y, while $\langle s_y \rangle$ to be antisymmetric [4]. This explains the features of the spin textures shown in Figure S1(b). The spin textures of the two other bands at the Fermi surface have the same symmetry properties.

As a result of these symmetries, the y-spin component averaged over the 2DBZ is expected to vanish, while the x-spin component is not. This is due to no symmetries in the magnetic space group enforcing the net (i.e. averaged over 2DBZ) $\langle s_x \rangle$ to disappear for the given magnetic structure shown Figure S1(a). As a result, a monocrystalline single-domain Mn_3Sn is expected to be spin polarized and be able to sustain a non-zero TMR effect in MTJs.

On top of the averaged finite $\langle s_x \rangle$ effect over the whole 2DBZ, MgO or any other amorphous or crystal tunneling barrier is expected to further select evanescent states of different $k_{\parallel}$, with the lowest decay rate within a circle around the 2DBZ center (the $\bar{\Gamma}$ point) [Fig. S1(b)]. With increasing MgO layer thickness, these states are concentrated closer and closer to the $\bar{\Gamma}$ point, thus selecting only a small region in the 2DBZ that is relevant. This alters the effective transport spin polarization in an MTJ compared to that in bulk Mn_3Sn.

The magnitude of the spin polarization from the AFM heavily depends on the crystal orientation [7]. Besides the (001) plane, other lower symmetry directions are not constrained by some of the symmetry restrictions discussed above, letting the spin polarization of both $\langle s_x \rangle$ and $\langle s_y \rangle$ be non-zero. It is also worth noting that the sign of TMR also depends on the AFM magnetic orientation. The symmetry ensures that the opposite domain (reversing all the Mn magnetic moment) leads to opposite spin polarization, which explains the opposite TMR polarity under opposite cooling field shown in Figure 4 (a) and (b) of the main text.

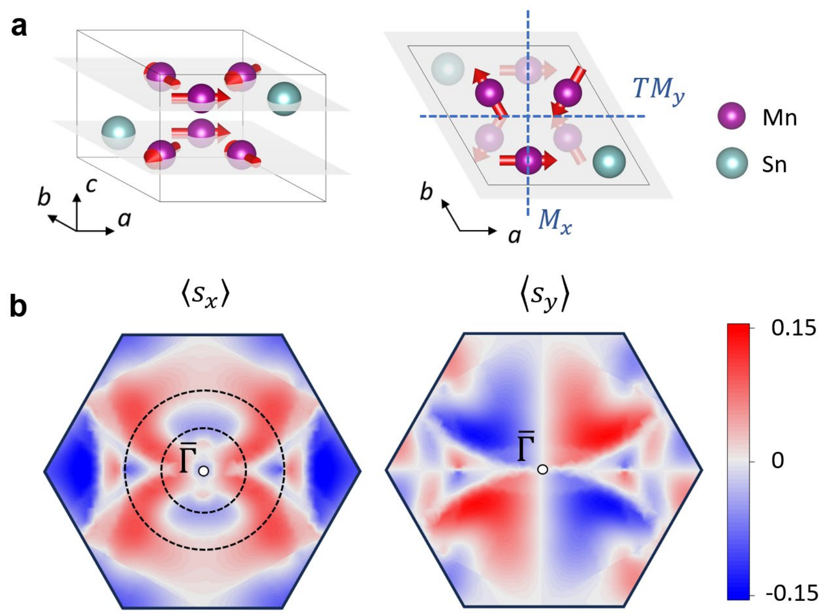

Supplementary Figure 1. $\boldsymbol{k}_\parallel$-dependent spin polarization of Mn_3Sn. (**a**) Atomic and magnetic structure of bulk Mn_3Sn: *left* – 3D view, *right* – projection to the (001) plane. Arrows indicate magnetic moments of Mn atoms. On the left panel, blue dash lines denote two planes perpendicular to the *a-b* plane, reflecting symmetry operations M_x and TM_y. (**b**) Expectation values of the spin components, $\langle s_x \rangle$ (left) and $\langle s_y \rangle$ (right), as a function of the in-plane wave vector $\boldsymbol{k}_\parallel = (k_x, k_y)$ in the (001) 2D Brillouin zone for one of the three Fermi surface sheets of bulk Mn_3Sn. Dashed circles indicate regions of $\boldsymbol{k}_\parallel$ corresponding to the states in Mn_3Sn that are expected to tunnel across the MgO barrier layer most efficiently for smaller (a large circle) and larger (a small circle) MgO layer thickness.

Section 2. Energy dispersive X-ray spectroscopy

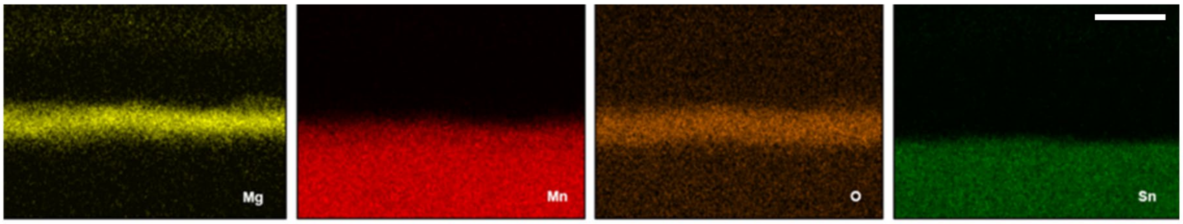

Supplementary Figure 2. Element distribution analysis by energy dispersive X-ray spectroscopy. Energy dispersive X-ray spectroscopy of the stack near the Mn_3Sn/MgO/CoFeB regions. The scale bar represents 10 nm for all four images.

Section 3. Grazing incidence X-ray diffraction of Mn3Sn

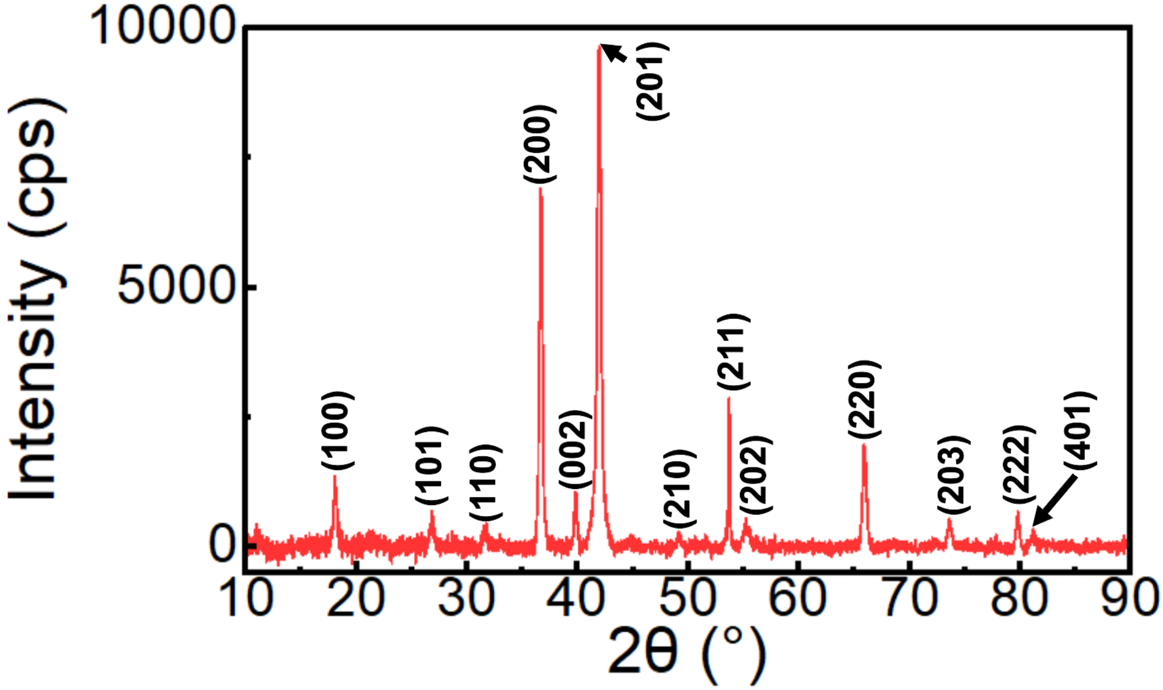

Supplementary Figure 3. Grazing incidence x-ray diffraction of Mn_3Sn. Each peak observed is well aligned with the peak position in the database. In addition, no additional peak is observed above the noise level, indicating no unwanted phase present in the film.

Section 4. Magnetization loop at room temperature

The magnetization-field curves are measured with SQUID-VSM technique in Quantum Design MPMS system. A linear background is subtracted from the raw data to account for the diamagnetism of the silicon substrate.

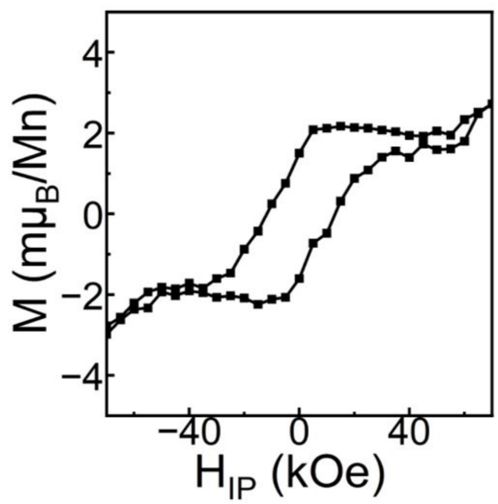

Supplementary Figure 4. Room temperature magnetization of Mn_3Sn. The saturation magnetization of Mn_3Sn at room temperature is roughly 2 $m\mu_B$.

Section 5. AHE shunting correction

The anomalous Hall resistance in Fig. 1f was measured with Ta/Ru cap. To calculate the anomalous Hall resistivity, shunting effect from the cap and seed layers have to be taken into account. The anomalous Hall conductivity is given by:

$$\rho_{xy} = R_{xy} \times t \times \left(\frac{\rho_{xx}}{t} \times \frac{1}{R_{xx}}\right)^2$$

where ρ_{xx}, ρ_{xy} is the longitudinal resistivity and Hall resistivity; R_{xx}, R_{xy} is the longitudinal sheet resistance and transverse resistance of the whole stack, respectively; t=50 nm is the Mn_3Sn thickness. R_{xx} is measured with Van der Pauw geometry to be 26 Ω/sq. Using the resistivity of Mn_3Sn in literature, 320 μΩ-cm, we obtained the corrected anomalous Hall resistivity of 2.1 μΩ-cm, which is close to values previous reports of polycrystalline Mn_3Sn [8].

Section 6. Large TMR in additional devices

TMR of different devices are shown in Fig. S5. The spread of TMR value is expected for devices made from polycrystalline Mn_3Sn since the spin polarization of AFM is dependent on its crystal orientation [9]. Similar spreads in TMR were also reported in the literature for symmetric AFMTJs [1, 10]. Nonetheless, the TMR of most devices shows large TMR comparable to FM tunnel junctions.

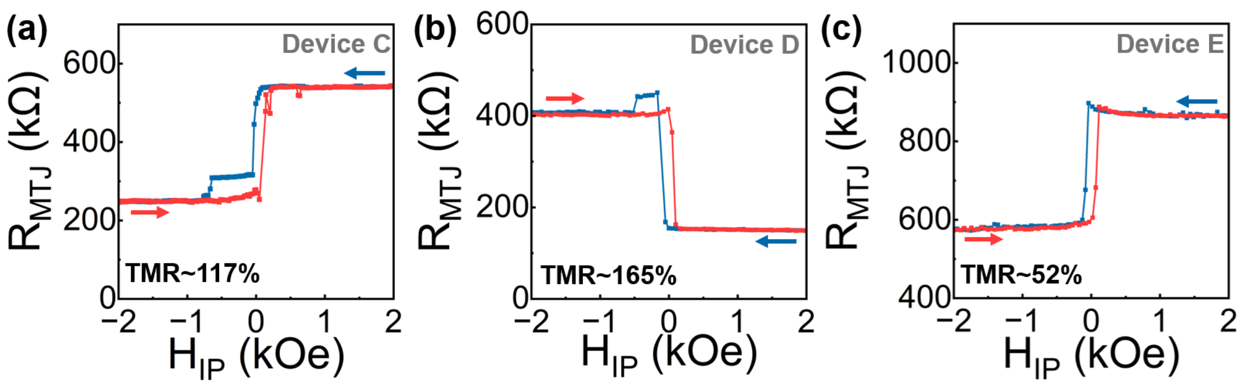

Supplementary Figure 5. Large TMR measured in additional devices. Tunneling magnetoresistance of additional Mn_3Sn/MgO/CoFeB tunnel junction devices (device C, D and E). All the data in this plot was from zero field cooling and therefore the polarity is random, consistent with Fig. 3b.

Section 7. Bias-dependence of the tunneling magnetoresistance

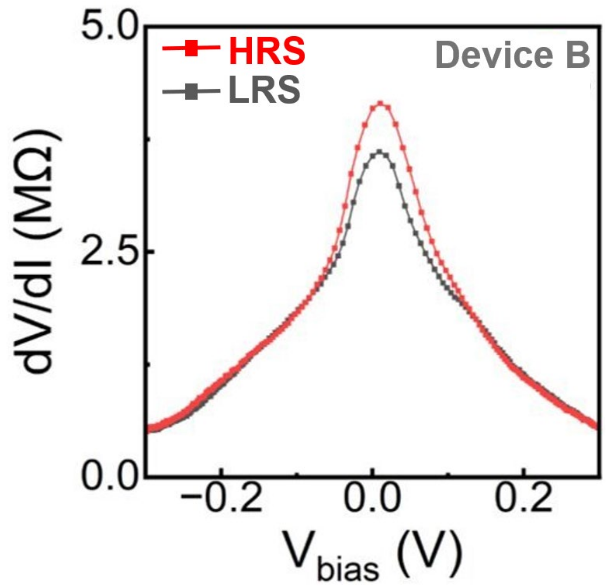

Supplementary Figure 6. AFMTJ resistance as a function of dc biasing voltage. The bias dependent TMR is measured using the same device as in Fig. 3. The high resistance state (HRS) and low resistance state (LRS) are measured under H_{IP} of -2 kOe and +2 kOe, respectively. Besides TMR, the low resistance state also exhibits a very strong biasing voltage dependence. This can be explained by the large tunneling barrier thickness of our AFMTJ, which leads to strong nonlinearity in the IV curve [11].

Section 8. Working mechanism of two types of AFMTJs

For a symmetric AFMTJ shown in Fig. S7a, the TMR originates from matching vs. mismatching of the local spin polarization in the reciprocal space of the two electrodes. In this case, the two electrodes are required to be crystallized in the same orientation for the TMR to be sizable. The tunneling current in the low resistance state consists of both spin up and spin down components as both spins see matching spin polarized states in the counter-electrode. Therefore, the tunneling current does not necessarily have a net spin polarization despite the junction shows sizable TMR. In comparison, in an asymmetric AFMTJ (as shown in Fig. S7b), one of the two spin direction is matched with high tunneling probability regions in the tunneling barrier (typically near the $\bar{\Gamma}$ point in the two-dimensional Brillouin zone). This matching effectively selects out one of the spin polarizations and leads to both TMR and net spin polarized tunneling current when paired with a ferromagnetic counter-electrode. Here we assume that the tunneling probability is higher for electrons that are close to the center of the project 2D Brillouin zone because they have a shorter effective tunneling length.

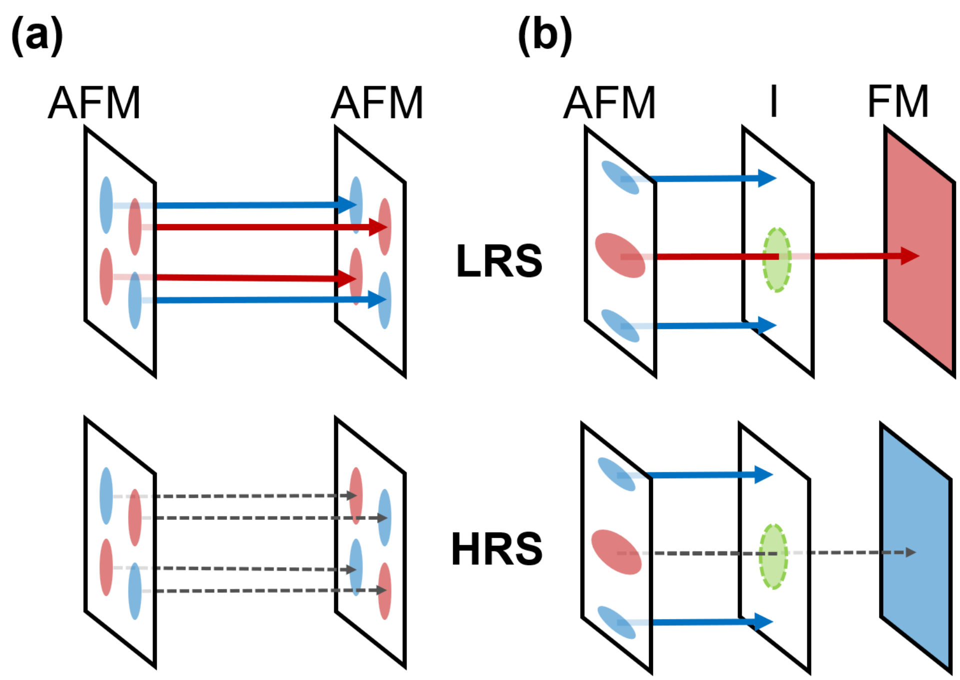

Supplementary Figure 7. Schematics of two types of AFMTJs. The working mechanism of symmetric (a) and asymmetric (b) AFMTJs. The red and blue regions indicate locally spin polarized states in the reciprocal space (see section 1 for the DFT calculation). The green region in (b) indicates regions with higher tunneling rate. The grey dashed arrows indicate forbidden tunneling due to mismatched spin polarization.

Section 9. Large field sweeps of the large TMR device

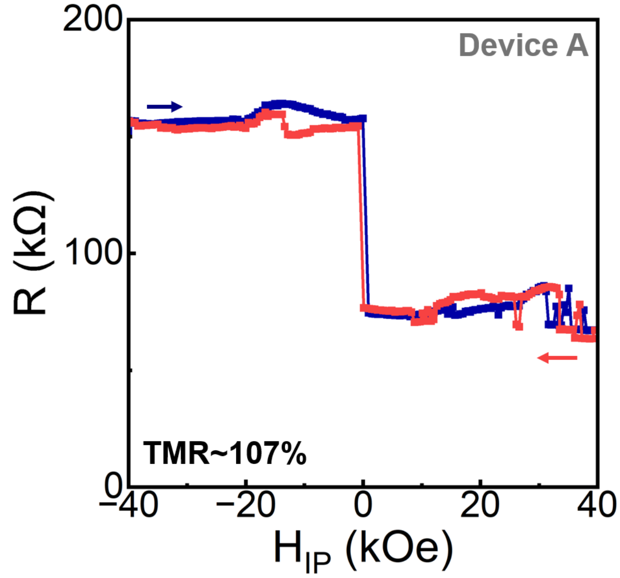

Supplementary Figure 8. Large field range tunneling magnetoresistance of an Mn_3Sn/MgO/CoFeB tunnel junction. The result shows that the 40 kOe minor loop feature in Fig. 3a is repeatable for different AFMTJs (Device A).

Section 10. Temperature dependence of TMR ratio

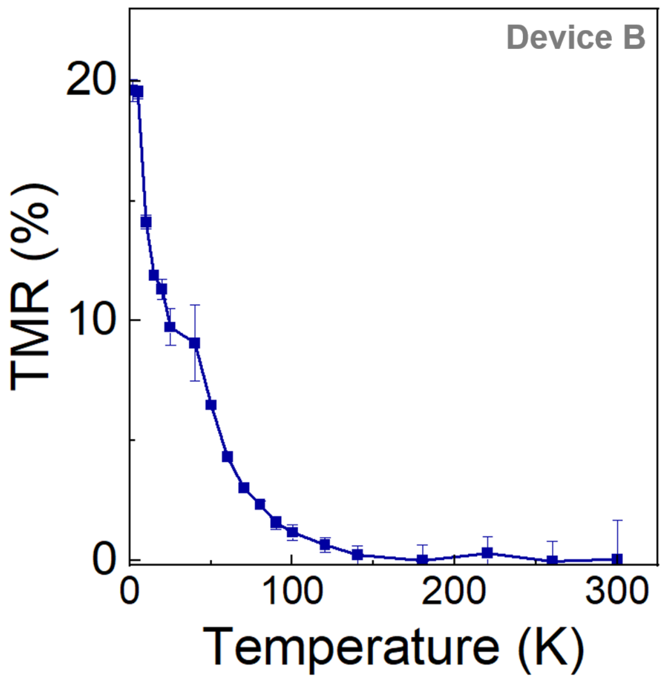

Supplementary Figure 9. Temperature dependence of TMR ratio. The TMR decreases with temperature and vanishes at temperatures above ~200 K. The error bars represent the standard deviation of the measured data.

Section 11. Temperature dependence of the magnetic moment offset

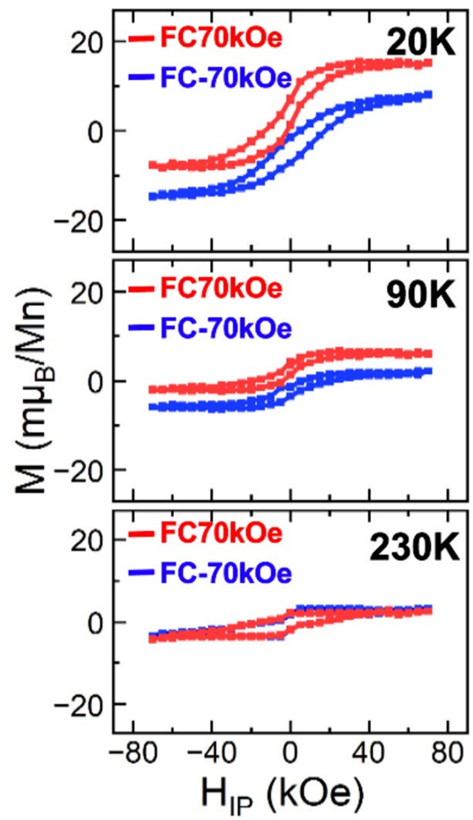

Supplementary Figure 10. Mn_3Sn magnetic moment offset measured at different temperatures. The red (blue) data are measured after cooling the Mn_3Sn under 70 kOe (-70 kOe) field. The magnitude of the offset drops to zero around 200 K.

Section 12. Mn_3Sn/CoFeB bilayer exchange bias

To check on the antiferromagnetic properties of the interfacial Mn_3Sn layer, we grow Mn_3Sn(50)/CoFeB(10) bilayers and study their exchange bias. The Mn_3Sn/CoFeB bilayer is cooled from RT to 10 K under ±500 Oe field and the magnetization (M-H) loop of the bilayer is measured. The magnetization switching in Fig. S11(b) corresponds to the CoFeB switching, which is offset by ~10 Oe in the opposite direction of the cooling field, indicating an exchange field H_E of 10 Oe acting on CoFeB. The exchange bias is a well-known indicator of the AFM phase in AFM/FM bilayer systems. This result thus confirms the AFM phase of Mn_3Sn interface at 10 K. Interestingly, we find that the exchange bias in our film vanishes after warming up to RT (Fig. S11a), suggesting a lower than RT blocking temperature in the AFM/FM bilayer, similar to un-pinning of the interfacial Mn_3Sn layer in our MTJs. Additional studies are necessary to show if there is an internal correlation between these two phenomena.

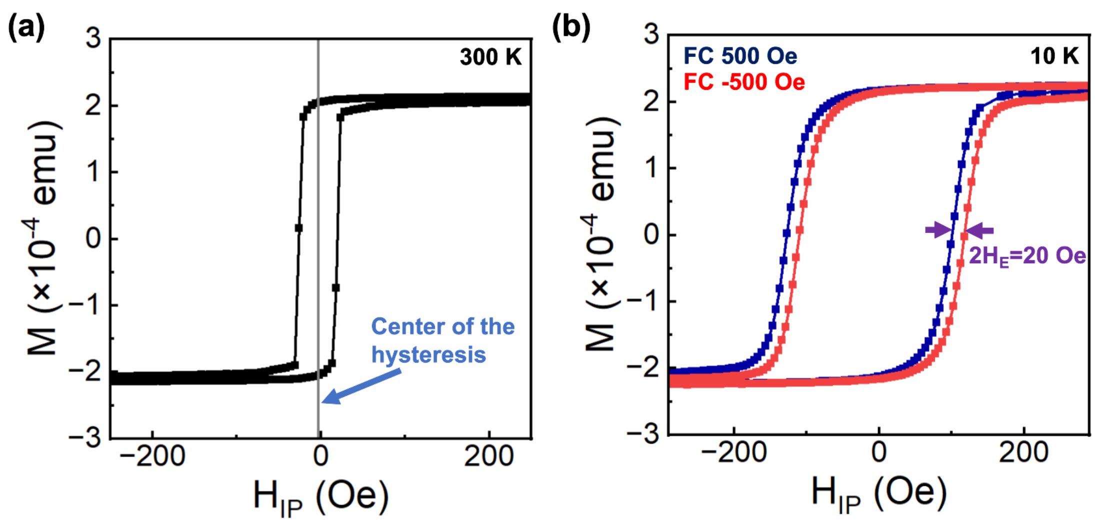

Supplementary Figure 11. Exchange bias of Mn_3Sn/CoFeB bilayers (a) M-H loop of Mn_3Sn/CoFeB bilayer at RT and (b) M-H loop after 500 Oe (blue) and -500 Oe (red) field cooling conditions. The M-H loop at RT is centered in (a), but a roughly 20 Oe offset is observed in (b) between the two field cooling conditions, which indicates exchange bias field H_E of 10 Oe in CoFeB.

Supplementary Reference

[1] Qin, P. et al. Room-temperature magnetoresistance in an all-antiferromagnetic tunnel junction. *Nature* **613**, 485–489 (2023).

[2] Gurung, G., Shao, D.-F. & Tsymbal, E. Y. Transport spin polarization of noncollinear antiferromagnetic antiperovskites. *Physical Review Materials* **5**, 124411 (2021).

[3] Giannozzi, G. et al., Quantum ESPRESSO: A modular and open-source software project for quantum simulations of materials. *J. Phys.: Condens. Matt.* **21**, 395502 (2009).

[4] Dong, J. et al. Tunneling magnetoresistance in noncollinear antiferromagnetic tunnel junctions. *Physical Review Letters* **128**, 197201 (2022).

[5] Gurung, G., Shao, D.-F. & Tsymbal, E. Y. Extraordinary tunneling magnetoresistance in antiferromagnetic tunnel junctions with antiperovskite electrodes. arXiv preprint arXiv:2306.03026 (2023).

[6] Shao, D.-F. & Tsymbal, E. Y. Antiferromagnetic tunnel junctions for spintronics. *npj Spintronics* **2**, 13 (2024).

[7] Zelenskiy, A., Monchesky, T., Plumer, M. & Southern, B. Anisotropic magnetic interactions in hexagonal a b-stacked kagome lattice structures: Application to Mn3X (X= Ge, Sn, Ga) compounds. *Physical Review B* **103**, 144401 (2021).

[8] Yoon, J. et al. Crystal orientation and anomalous hall effect of sputter-deposited non-collinear antiferromagnetic mn3sn thin films. *Applied Physics Express* **13**, 013001 (2019).

[9] Železnỳ, J., Zhang, Y., Felser, C. & Yan, B. Spin-polarized current in noncollinear antiferromagnets. *Physical Review Letters* **119**, 187204 (2017).

[10] Chen, X. et al. Octupole-driven magnetoresistance in an antiferromagnetic tunnel junction. *Nature* **613**, 490–495 (2023).

[11] Simmons, J. G. Generalized formula for the electric tunnel effect between similar electrodes separated by a thin insulating film. *Journal of Applied Physics* **34**, 1793–1803 (1963).